Electrochimica Acta 441 (2023) 141759

Contents lists available at ScienceDirect

Electrochimica Acta

journal homepage: www.journals.elsevier.com/electrochimica-acta

Local structure transformations promoting high lithium diffusion in defect perovskite type structures

William R. Brant [a,#,*], Tatiana Koriukina [a], Yu-Chuan Chien [a], Holger Euchner [b], Jesus Sanz [c], Alois Kuhn [d], Ralf Heinzmann [e], Sylvio Indris [e], Siegbert Schmid [b,f,*]

[a] Department of Chemistry – Ångström Laboratory, Ångström Advanced Battery Centre, Uppsala University, Box 538, Uppsala SE-751 21, Sweden
[b] Helmholtz Institute Ulm (HIU) Electrochemical Energy Storage, Helmholtzstr. 11, Ulm 89081, Germany
[c] Instituto de Ciencia de Materiales de Madrid ICMM-CSIC, C/Sor Juana Inés de la Cruz 3, 28049, Cantoblanco, Madrid, Spain
[d] Departamento de Química y Bioquímica, Facultad de Farmacia, Universidad San Pablo-CEU, CEU Universities, Madrid 28668, Spain
[e] Karlsruhe Institute of Technology (KIT), Institute for Applied Materials (IAM), Hermann-von-Helmholtz-Platz 1, Eggenstein-Leopoldshafen 76344, Germany
[f] School of Chemistry, The University of Sydney, Sydney, NSW 2006, Australia

ARTICLE INFO

Keywords:
Local structure
^{7}Li NMR
Defect perovskite
Intermittent current interruption technique

ABSTRACT

Defect perovskites, A_xBO_3 such as $(Li_{3x}La_{2/3-x})TiO_3$, are attracting attention as high capacity electrodes in lithium-ion batteries. However, the mechanism enabling high lithium storage capacities has not been fully investigated. In this work, the reversible insertion and removal of lithium up to an average *A*-site cavity occupancy of 1.71 in the defect perovskite $(Li_{0.18}Sr_{0.66})(Ti_{0.5}Nb_{0.5})O_3$ is investigated. It was shown that subtle lithium reorganization during lithiation has a significant impact on enabling high capacity. Contrary to previous studies, lithium was coordinated to triangular faces of Ti/Nb oxygen octahedra and offset from O_4 windows between *A*-site cavities in the as-synthesised material. Upon electrochemical lithiation Li-Li repulsion redistributes of all the lithium towards the O_4 window position resulting in a loss of lithium mobility. Surprisingly, the mobility is regained during over-lithiation and following multiple electrochemical cycles. It is suggested that lithium reorganisation into the center of the O_4 window alleviates the Li-Li repulsion and modifies the diffusion behavior from site percolation to bond percolation. The results obtained provide valuable insight into the chemical drivers enabling higher capacities and enhanced diffusion in defect perovskites. More broadly the study delivers fundamental understanding on the non-equilibrium structural transformations occurring within electrode materials during repeated electrochemical cycles.

1. Introduction

During the past few decades Li-ion batteries (LIBs) have undeniably proven themselves as one of the most efficient and reliable energy storage devices. Yet, work continues on improving the current design and modifying materials to be matched with the desired end application of the battery. Specific areas of research interest towards this today include improving the capacity of the electrodes and designing materials that enable the use of lithium metal as a negative electrode, such as solid state electrolytes. A material class which bridges the gap between high capacity electrodes and solid state electrolytes are defect perovskites. Defect perovskite oxides are a versatile class of materials which have previously been investigated as solid state electrolytes for LIBs. Specifically, the material class was first recognized following the discovery of remarkably high ionic conductivity of 1×10^{-3} S cm^{-1} for $(Li_{3x}La_{2/3-x}\square_{1/3-2x})TiO_3$ (where $\square$ represents a vacancy) in 1993 [1]. Thanks to the open structure and compositional tuneability they are also very interesting as electrode materials.

Perovskite oxides can be described by the general formula ABO_3, whereby large *A*-site cations fill the cuboctahedral cavities created by the three-dimensional network of corner linked BO_6 octahedra (Fig. 1A). Compositional variability enabled by structural flexibility allows for a wide variety of cation combinations, including the exclusion of *A*-site cations altogether creating a large vacant site, through which small cations are able to rapidly diffuse. This feature of the perovskite structure led to the first studies of lithium lanthanum titanates, $Li_{3x}La_{2/3-x}\square_{1/}$

* Corresponding authors.
E-mail addresses: William.brant@kemi.uu.se (W.R. Brant), siegbert.schmid@sydney.edu.au (S. Schmid).
Current address: Department of Chemistry – Ångström Laboratory, Ångström Advanced Battery Centre, Uppsala University, Box 538, SE-751 21 Uppsala, Sweden.

https://doi.org/10.1016/j.electacta.2022.141759
Received 6 October 2022; Received in revised form 25 November 2022; Accepted 22 December 2022
Available online 23 December 2022

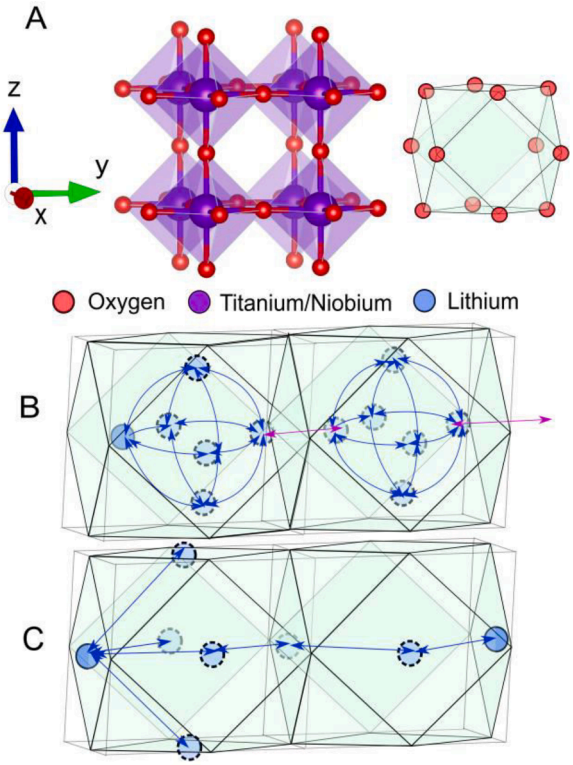

Fig. 1. A: Fragment of the *A*-site deficient perovskite unit cell showing the coordination of the BO_6 octahedra. The vacant cuboctahedron formed from the corner linked BO_6 octahedra is shown to the right. **B:** Diffusion pathway for Li^+ ions between two cuboctahedra via a site percolation mechanism and **C:** Diffusion pathway for Li^+ ions via a bond percolation mechanism. In the latter case all jump paths of the first lithium ion are shown, and then only one possible conduction path is drawn thereafter. The oxygen atoms are not shown for clarity. Blue arrows show fast lithium hopping paths and the pink arrows indicate relatively slower hopping paths.

$_{3-2x}TiO_3$ or LLTO as solid state ionic conductors in 1987 by Belous et al. [2] which was further optimized by Inaguma et al. in 1993 [1]. Since then extensive work has been performed exploring the origins of such high ionic conductivity and the possibility to implement defect perovskites as solid ionic conductors. Based on these early investigations it was proposed that Li^+ conducted via site percolation. That is, within the *A*-sites there is a high degree of Li^+ mobility, however, long range diffusion only occurs via Li^+ hopping between vacant *A*-site cavities which is comparatively slower (Fig. 1B). This model implies that significant diffusion could only occur if there were $\geq$ 0.34 vacant *A*-sites ensuring a continuous diffusion pathway through the cubic structure. This places strict requirements on material composition [3]. Furthermore, the main barriers to Li^+ diffusion were identified to be the size of vacant sites [4], the oxygen windows acting as bottleneck between vacant sites [5,6] and the strength of lithium and oxygen bonding [7].

One of the challenges encountered while deploying LLTO in Li-metal batteries was its instability on contact with metallic lithium, when it undergoes easy and fast Li^+ insertion with concurrent reduction of Ti^{4+} to Ti^{3+}, leading to high electronic conductivity [1,8–10]. However, the discovery of Ti^{4+}/Ti^{3+} reductive insertion of Li^+ into the structure raised interest in using LLTO and similar perovskites as electrodes for Li-ion rechargeable batteries. First reports on electrochemical Li^+ insertion at potentials from 1.7 V to ~0.6 V showed the possibility to insert 0.15 Li^+ per formula unit (FU) of $La_{0.56}Li_{0.33}TiO_3$ [11,12] and 0.14 Li^+ per FU of $La_{0.57}Li_{0.29}TiO_3$ [9]. Given that there remained both space in the structure and reducible cations, the possibility to extend the capacity by cycling to lower potentials existed. Chen and Amine [13] were the first to demonstrate that it was possible to host significantly more than 1 Li^+ per available *A*-site cavity when lithiated to 0 V. An available *A*-site is considered to be one that is either vacant, or occupied by a mobile cation. Specifically, $La_{0.55}Li_{0.35}TiO_3$ was able to reversibly insert 0.48 Li^+ per FU which corresponds to an average Li^+ A-site occupancy of 1.84. The concept of inserting more than one Li^+ ion per available *A*-site during lithiation in a battery will from here on be referred to as "over-lithiation".

Interestingly, this ability to reversibly and topotactically insert multiple lithium ions per available *A*-site contradicts predictions based on site percolation theory which states that ion conduction should decrease sharply once each *A*-site is occupied by a cation [3,14]. In contrast, it has been demonstrated on multiple occasions that perovskites are able to host a larger quantity of lithium in the structure. For example, $Li_{1.5}La_{1.5}WO_6$ [15] shows a reversible capacity of ~125 mAh g^{-1}, and computational modelling predicts that up to 4 Li^+ can occupy a single *A*-site of $Li_{3.0}La_{1.5}WO_6$ during over-lithiation. More recently LLTO was reported as a negative electrode material [16] exhibiting a reversible capacity of ~225 mAh g^{-1} at 1C rate over 3000 cycles. While a portion of the capacity was suggested to arise from the intrinsic pseudocapacitance of the material, it demonstrates that a high concentration of lithium can be reversibly inserted into the structure.

The possibility of significant ion conduction beyond the percolation limit has been considered previously. For perovskites adopting orthorhombic and tetragonal symmetries with Li^+ located within the *A*-site cavity, Li^+ conduction between the neighboring vacant *A*-site cavities can be described by the site percolation model [3,17]. However, for perovskites adopting orthorhombic and rhombohedral symmetry with Li^+ sitting within the O_4 windows between the cubotahedral *A*-site cavities, the site percolation model was insufficient to describe the Li^+ mobility and instead a bond percolation model was suggested [18–21]. The key difference is that Li^+ ion diffusion pathways lie between the face centers of two neighbouring O_4 windows. Thus, for one Li^+ ion within the O_4 window, there are eight nearby sites in two adjacent *A*-site cavities into which it can migrate. Four of these paths are shown in Fig. 1C. However, lithium migration does not occur via O_4 sites adjacent the highly charged La^{3+} cation, which subsequently has an impact on Li^+ ion mobility. Thus, perovskite ion conductors incorporating *A*-site cations of a lower charge, such as Sr^{2+} may exhibit further improved conduction properties for higher lithium contents. To this end, the $Li_{2y}Sr_{1-x-y}Ti_{1-2x}Nb_{2x}O_3$ (LSTN) family of compounds were investigated as an alternative. The larger ionic radius of Sr^{2+} creates larger *A*-site cavities and is anticipated to improve conductivity. Further, many previously investigated Sr^{2+} based defect perovskites form cubic structures with a random distribution of entities occupying the *A*-site leading to three-dimensional diffusion pathways [22,23].

Within the LSTN family, $Li_{0.18}Sr_{0.66}Ti_{0.5}Nb_{0.5}O_3$ (L018STN) is an exemplary case to consider in the context of understanding changing lithium mobility during over-lithiation. Previous research has shown that the most likely location for Li^+, and by extension the most likely diffusion pathway, is a curved path around the *A*-site cavity linking together the O_4 windows [22]. However, the Li^+ ions are not located within the O_4 site but rather within the *A*-site cavity. While most of the Li^+ ions in the as-synthesised material could not be located using diffraction data due to either static or dynamic (i.e. diffusion) disorder, some could be modelled at a position slightly off-set from the O_4 window. Following chemical Li^+ insertion to a composition $Li_{0.4}Sr_{0.66}Ti_{0.5}Nb_{0.5}O_3$ (1.18:1 Li:available *A*-site) Li^+ was found within the O_4 window. Interestingly, preparing a similar sample via electrochemical insertion resulted in Li^+ sitting slightly offset from the O_4 window site [24], however, if L018STN is potentiostatically held at 1 V Li^+ begins to migrate into the O_4 window [25]. The changing Li^+ position during Li^+ insertion is likely to impact the nature of lithium diffusion from being best described by site percolation to bond percolation during over-lithiation. However, the connection between lithium reorganization and its mobility has not yet been determined.

In this study the structure, and in particular lithium position, during

electrochemical lithium insertion is investigated more closely using a combination of neutron diffraction and ^{7}Li magic-angle spinning nuclear magnetic resonance (MAS NMR) spectroscopy, whereas the lithium mobility is monitored during galvanostatic cycling using the intermittent current interruption technique. Observing the evolution of lithium mobility over many cycles and comparing to previous and new measurements of the changing lithium position, supports a new lithium migration mechanism, which explains the enhanced lithium mobility over multiple cycles.

2. Experimental

2.1. Synthesis and electrode preparation

Polycrystalline samples of $Li_{0.18}Sr_{0.66}Ti_{0.5}Nb_{0.5}O_3$ (L018STN) were prepared by heating stoichiometric quantities of Li_2CO_3 (Merck, 99 %), $SrCO_3$ (Aldrich, 99.9+ %), TiO_2 (Aithaca, 99.995 %) and Nb_2O_5 (Aithaca, 99.998 %) to 950°C for 15 hours. Finally, prepared pellets were heated at 1190°C for 48 hours and quenched in air. The surface morphologies of the as-prepared L018STN powder and pristine L018STN electrodes were studied using SEM (Leo 1550, Zeiss).

Electrodes for *ex situ* measurements using ^{7}Li MAS NMR spectroscopy were prepared by grinding the sample with conducting carbon black by using a planetary-type ball mill Pulverisette 7 (Fritsch GmbH, Germany) in order to obtain a homogeneous carbon-metal oxide composite. Ball milling was performed in a 20 ml zirconium dioxide jar with two 10 mm zirconium dioxide balls. Dry milling was run at 500 rpm for 1 hour in air. The composite mixture was then mixed with polytetrafluoroethylene (PTFE) (Aldrich) as a binder. The mixture contained 75 % L018STN sample, 20 % conducting carbon black and 5 % PTFE. Positive electrode pellets 8 mm in diameter using 25-30 mg of the mixture were pressed for the NMR experiments. Swagelok-type cells were assembled in an Ar glovebox with Li-foil as negative electrode and glass-fibre separator soaked with 1 M $LiPF_6$ in 1:1 (v/v) ethylene carbonate:dimethyl carbonate (EC:DMC). Electrochemical lithium insertion was performed using a BioLogic VMP multichannel potentiostat. Samples were galvanostatically cycled to the desired potential cut-off, the electrode removed from the cell and crushed up in a vial containing DMC (Sigma-Aldrich $\geq$ 99 %). The resulting powders were rinsed three times with DMC and dried and stored under Ar (H_2O, $O_2 < 1$ ppm).

Electrodes for long term electrochemical cycling and X-ray photoelectron spectroscopy analysis were prepared by mixing active material, carbon black (Super C65, Imerys) and polyvinylidene fluoride (PVDF, Kynar PVDF HSV 900) in a 80:10:10 weight ratio in an appropriate amount of N-methyl-2-pyrrolidone (NMP $\geq$99.5%, GPR RECTAPUR) in a mixer mill to form a slurry. The slurry was then cast onto a 20 μm thick copper sheet with a 100 μm notch bar. The NMP was evaporated by keeping the cast electrode at 70°C for 2 hours and then at room temperature overnight. Electrodes of 13 mm diameter where then punched from the resulting coating. The active material mass loading of obtained electrodes varied between 5.5-6 mg cm^{-2}. Prior to the assembly, composite electrodes were dried in a vacuum oven inside the glovebox at 120°C for 15 hours. Electrodes were cycled in polymer-coated aluminum pouch cells using Celgard 2325 as separator soaked in LP40 electrolyte (1 M $LiPF_6$ in 1:1 vol EC:DEC mixture, (Gotion)) and a 15 mm diameter disc of Li-metal foil as a combined reference and counter-electrode. Copper strip placed in contact with lithium metal and aluminum strip in contact with composite electrode copper film were used as current collectors. Cells were assembled and sealed in an argon filled glovebox (H_2O, $O_2 < 2$ ppm).

2.2. Electrochemical tests

Charge/discharge processes in a Li-ion cell are usually described such that during discharge the positive electrode is lithiated and the cell voltage is reduced. On charge the opposite applies. Since all of our electrochemical tests were performed in a half cell design, i.e. vs Li-metal, Li was the negative electrode, while L018STN was utilised as the positive electrode. Discharge would thus correspond to lithiation of L018STN and charging delithiation. To remove ambiguity the terms "lithiation" and "delithiation" of L018STN are used throughout the manuscript.

Cyclic voltammetry was performed on a Biologic SP300 potentiostat with a scan rate of 0.5 mV/s for 5 cycles from ~3 V to 0.25 V on the first lithiation and then reversed up to 2.5 V on charging for subsequent cycles. The galvanostatic cycling was coupled with the intermittent current interruption (ICI) method, which introduced periodic transient current pauses [26]. By analysing the potential change (ΔE) during the current interruption, an internal resistance (R), representing the sum of electronic, ionic, and charge-transfer resistance, and a diffusion resistance coefficient (k), can be obtained from the following relationship.

$$\Delta E(t) = -IR - Ik\sqrt{t}$$

where t is the time since current is switched off. The diffusion resistance coefficient is proportional to the coefficient of a Warburg element (σ) used in electrochemical impedance spectroscopy (EIS) [27] and can thus be used to deduce the chemical diffusion coefficient of Li^+ (D_{Li+}) in an insertion electrode material following Eq. 1 according to the previously reported method [28].

$$D_{Li^+} = \frac{4}{\pi}\left(\frac{V}{S}\frac{\frac{dE_{OC}}{dt_I}}{Ik}\right)^2 \quad (1)$$

where V is the molar volume, S is the electrochemically active surface area, dE_{OC}/dt_I is the derivative of open-circuit potential (OCP) with respect to the time where the current is applied, which is approximated in the ICI method by the IR-drop corrected pseudo-OCP slope [28]. Here, due to the uncertainty of the electrochemical active surface area of the sample in composite electrodes, a Li^+ mobility ($m_{Li} = D_{Li+}S^2V^{-2}$) is reported, which is appropriate for the comparison of Li^+ diffusion in the same electrode at different states of charge.

$$m_{Li^+} = \frac{4}{\pi}\left(\frac{\frac{dE_{OC}}{dt_I}}{Ik}\right)^2 \quad (2)$$

Using an Arbin battery tester, a constant current of 0.1 mA cm^{-2} was applied with a one-second current pause every five minutes. The cells were cycled from an open circuit voltage (OCV) of ~3 V to 0.25 V on the first lithiation and then reversed up to 3 V on charging for subsequent cycles. By analyzing the potential response to a current pause, information on cell resistance is derived continuously over 70 lithiation/delithiation cycles. The application of the ICI method on the studied material is validated by the accompanying EIS measurements in the selected cycle in Fig. S1 with the EIS data shown in Fig. S2.

EIS data on pristine L018STN powder was collected in a two-electrode Swagelok cell with stainless steel blocking electrodes. Before the measurement ~0.7 mg L018STN powder was pelletised into a 13 mm pellet with the thickness of 1.35 mm. The pellet underwent sintering at 700°C for 5 hours, heating was performed in air from 20°C to 700°C at 5°C/min and cooled inside the furnace from 700°C to 20°C at 5°C/min. Electrochemical impedance spectroscopy measurements were conducted with a Schlumberg SI 1260. EIS spectrum was collected at 298 K until reproducible for 3 times from 7 MHz to 100 mHz, the amplitude of the AC signal was 20 mV. The data was fitted to an equivalent circuit and the ionic conductivity was calculated from the bulk resistance R_0.

2.3. Neutron powder diffraction (NPD)

Neutron powder diffraction patterns for the as-synthesised L018STN

were obtained using the ECHIDNA high resolution powder diffractometer at the OPAL reactor, Australian Nuclear Science and Technology Organisation [29]. Diffraction patterns were collected at 6 K using a top loading AS Scientific Cryofurnace and a wavelength of 1.622 Å.

2.4. X-ray photoelectron spectroscopy (XPS)

The XPS measurements were performed on electrodes *ex situ* using a PHI 5500 X-ray Photoelectron Spectrometer with an Al source utilizing K_α radiation (1486.6 eV), an electron emission angle of 45°, pass energy 23.5 eV, step size 0.1 eV and time per step – 100 ms. Electrodes were galvanostatically cycled to the chosen potentials (first cycle) and potentiostatically held there for several hours. The electrodes were then extracted from cells and washed with DMC in an argon filled glovebox (H_2O, $O_2 < 1$ ppm). Transfer of the electrodes into the XPS machine was made using an inert transfer shuttle, avoiding exposure of the electrodes to air. XPS data were analyzed with CASA XPS software [30] and the hydrocarbon peak at 284.8 eV was used for calibration. The ratio between the areas of 2p 1/2 Ti^{+4} and 2p 1/2 Ti^{+3} peak was used to evaluate the ratio between Ti^{+4} and Ti^{+3} species. The ratio between the areas of 3d 5/2 Nb^{+5} and 3d 5/2 Nb^{+4} peaks was used to evaluate the ratio between Nb^{+5} and Nb^{+4} species.

2.5. ^{7}Li NMR spectroscopy

^{7}Li magic angle spinning (MAS) NMR spectra were recorded at room temperature using AVANCE 200 ($B_0 = 4.7$ T) and AVANCE 400 ($B_0 = 9.4$ T) Bruker spectrometers working at 77.75 and 155.50 MHz, respectively. The as-synthesised powder was analysed on the AVANCE 400 spectrometer after single pulse irradiation of 1.75 μs with a recycling time of 1 s. Samples were spun at 10 kHz in 2.5 mm ZrO_2 rotors. The number of scans was chosen to obtain signal/noise ratios higher than 10. The electrochemically prepared samples were measured on the AVANCE 200 spectrometer using 2.5 mm zirconia rotors at 25 kHz in a dry nitrogen atmosphere. The typical values for the recycle delay and the $\pi/2$ pulse length were 5 s and 2 µs, respectively. In both cases an aqueous 1 M LiCl solution was used as ^{7}Li chemical shift reference.

2.6. DFT calculations

Density functional theory (DFT) calculations have been conducted using the Vienna ab initio simulation package (VASP) [31,32]. Spin polarized calculations were conducted using the projector augmented wave method, while exchange and correlations were described with the generalized gradient approximation [33]. As starting configuration a 3 × 4 × 3 perovskite supercell with 174 atoms and $Li_{0.17}Sr_{0.67}Ti_{0.5}Nb_{0.5}O_3$ stoichiometry was constructed (Fig. S3A), almost perfectly matching the experimental stoichiometry of L018STN. To account for the inherent disorder of the perovskite, the special quasirandom structure (SQS) approach as introduced by Zunger was used for the supercell creation via the atat package [34,35]. SQS structures allow treatment of disorder by using realistic configurations in a comparably small supercell. Moreover, starting from this supercell, structures with increased Li-contents have been investigated. This was achieved by filling all vacant cavities by one Li atom (Fig. S3B) (i.e. each *A*-site was either occupied by Li or by Sr: $Li_{0.33}Sr_{0.67}Ti_{0.5}Nb_{0.5}O_3$) or two Li atoms (Fig. S3C) (i.e. each vacant *A*-site was occupied by two Li atoms: $Li_{0.5}Sr_{0.67}Ti_{0.5}Nb_{0.5}O_3$). Finally, a structure was constructed with each *A*-site that is not occupied by Sr being filled by two Li atoms (Fig. S3D) (i.e. $Li_{0.67}Sr_{0.67}Ti_{0.5}Nb_{0.5}O_3$ stoichiometry). For structural optimization, the different configurations were relaxed with respect to lattice parameter and atomic coordinates, applying a plane wave cutoff of 600 eV and a 3 × 3 × 3 k-point mesh.

Furthermore, ab initio MD (AIMD) calculations were performed for the optimized supercells with $Li_{0.17}Sr_{0.67}Ti_{0.5}Nb_{0.5}O_3$ and $Li_{0.5}Sr_{0.67}Ti_{0.5}Nb_{0.5}O_3$ stoichiometry. The AIMD runs were performed to investigate the dynamics of the Li atoms within the compound, applying a NVT ensemble with a cutoff energy of 500 eV and a 1 × 1 × 1 k-point mesh. After equilibration, the simulations were conducted for about 50 ps (at least 10,000 steps with a 5 fs time step).

3. Results

3.1. Lithium position in as-synthesised L018STN

The L018STN powder used in this study is the same as that reported previously [22,25]. In those previous studies X-ray diffraction (XRD) revealed a pure cubic ($Pm\bar{3}m$) perovskite type structure and elemental analysis provided a composition of $Li_{0.183(2)}Sr_{0.69(2)}Ti_{0.54(1)}Nb_{0.5(1)}O_3$. The absence of *A*-site ordering suggests a three-dimensional Li diffusion pathway. Here, SEM imaging revealed the as-synthesised powder to be polycrystalline with the largest particles on the order of 10 µm (see Fig. S7A and B for SEM images). The ionic conductivity of a sintered L018STN pellet extracted from EIS measurements at 298 K (see Fig. S8 for the fit) was found to be 3.0±2.3 × 10^{-6} S cm^{-1} which is lower in comparison with that previously reported for $(Li_{3x}La_{2/3-x}\square_{1/3-2x})TiO_3$ (1 × 10^{-3} S cm^{-1}) [1].

To answer the question of how Li^+ relocates during Li^+ insertion, its position must first be determined in the pristine sample. While this has been investigated previously [22,25], a common result is the total lithium content determined via elemental analysis exceeds the amount modelled via the Rietveld method applied to diffraction data. This suggests that there remains Li^+ present in the structure which is unaccounted for, either due to a high degree of static (positional) or dynamic (Li^+ hopping) disorder. Thus, neutron diffraction was performed at 6 K to reduce thermally induced dynamic disorder.

The neutron diffraction data were analysed by first fitting a model without lithium and calculating Fourier difference maps. The negative neutron scattering length of lithium (-1.9 fm) increases the contrast in Fourier difference maps relative to the other positive scattering elements in its proximity. The structural model was subsequently updated to include lithium at detected positions and the Fourier map recalculated. The diffraction pattern fitted with the new model is given in Fig. S4. Contrary to the result obtained for L018STN at room temperature [22] there was significant negative scattering observed near the oxygen window and in close proximity to the Ti/NbO_6 octahedral face (Fig. 2A). In order to establish the best position for lithium, three models were tested (Fourier difference maps given in Fig. 2). The first model contained lithium refined to the 6f site (0.5 0.5 0.15), offset from the oxygen window, coordinated by four oxygen atoms (Li1 in Table 1). The second model contained lithium refined to the 8g site (0.29 0.29 0.29), near the Ti/NbO_6 octahedral face and coordinated by three oxygen atoms (Li2 in Table 1). The third model had lithium distributed over the 6f and 8g sites, with the total content constrained to the values determined by ICP-AES analysis. While the first two models were stable, the third containing two lithium sites was not, resulting in negative atomic displacement parameters (ADPs) for lithium, so it was discarded. Data for the lithium free and lithium containing models are presented in Table 1. Both models resulted in a refined Li^+ occupancy per FU (occ/FU) that was within error of the expected composition. The model with lithium on the Li2 position provided a slightly improved Bragg R factor (R_B) and a greater improvement in the Fourier difference map (Fig. 2C). In comparison, the Li1 model converged with a slightly high ADP value for lithium, indicating that some positional disorder exists around this site.

Observation of a lithium position between the O_4 windows and offset from the MO_6 octahedral face is somewhat unexpected but not unreasonable. It has been observed previously for the perovskite $La_3Li_3W_2O_{12}$ [36] and the site falls within a favourable region for lithium based on bond-valence calculations [22]. On the other hand, considering electrostatic repulsions in terms of charge and proximity between Li^+ and

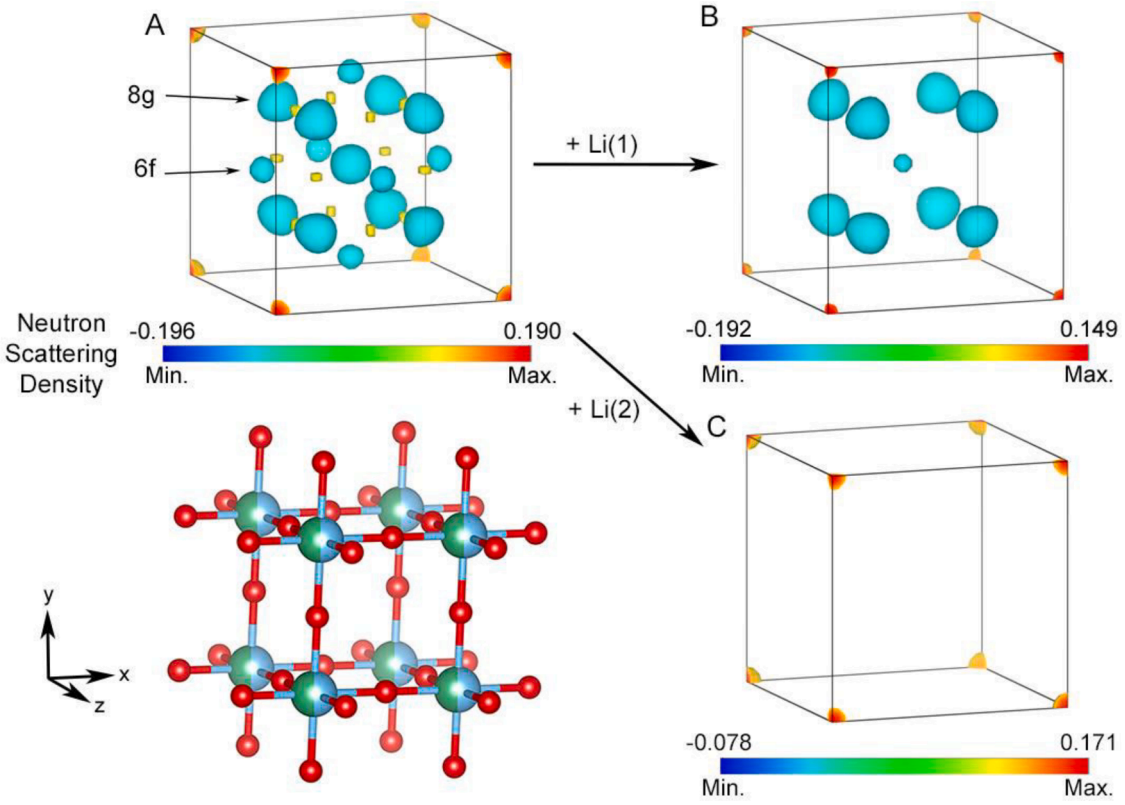

Fig. 2. Fourier difference maps before (A) and after including lithium in the L018STN model on the Li1(6f, B) and Li2(8g, C) positions respectively. An intensity cut-off of 0.12 was used in every case to remove low intensity noise. A picture of the structure around an *A*-site is provided for reference.

Table 1
Comparison of refined parameters between the three different models fit to the NPD data collected at 6 K. The Li1 model contains lithium on the 6f site with position coordinates x = y = 0.5. The Li2 model contains lithium on the 8g site where x = y = z. Anisotropic ADPs were refined for oxygen.

L018STN @ 6 K $Pm\bar{3}m$, a = 3.93042(2) Å			
	Li Free	Li1 model	Li2 model
R_B (%)	1.75	1.64	1.54
χ^2	1.66	1.65	1.64
ADPs (Å^2)			
Sr	0.0053(5)	0.0053(5)	0.0056(5)
Ti/Nb	0.019(1)	0.019(1)	0.021(1)
O (U_{11})	0.0019(6)	0.0016(6)	0.0011(6)
O (U_{22})	0.0116(4)	0.0115(4)	0.0118(4)
Li	N/A	0.07(4)	0.01(1)
Li (occ/FU)	N/A	0.14(5)	0.22(3)
Li (z)	N/A	0.15(3)	0.29(1)

next nearest cations, Li^+ cations are less stabilized in Li^+-$3O^{2-}$-Ti^{4+} or Li^+-$3O^{2-}$-Nb^{5+} (8g site) configurations than in Li^+-$4O^{2-}$-Sr^{2+}, Li^+-$4O^{2-}$-Li^+ or Li^+-$4O^{2-}$-vac (6c site). Thus, the lithium occupation of sites coordinated by three oxygen atoms could be less favorable than the four coordinated site. However, some of the electrostatic repulsion may be alleviated by the lithium migrating away from the octahedral face towards the cuboctahedral cavity center (0.5 0.5 0.5 site). It is also possible that some degree of static positional disorder exists at 6 K with the majority of lithium located away from the O_4 window site. By extension, at room temperature there is likely rapid hopping of lithium between the 6f and 8g sites. To explore this possibility, ^{7}Li NMR at room temperature was performed.

The central line of the ^{7}Li NMR spectrum of the as-prepared material, shown in Fig. 3, is composed of two peaks at 0.52 ppm and 1.97 ppm revealing the existence of two lithium environments. The small positive

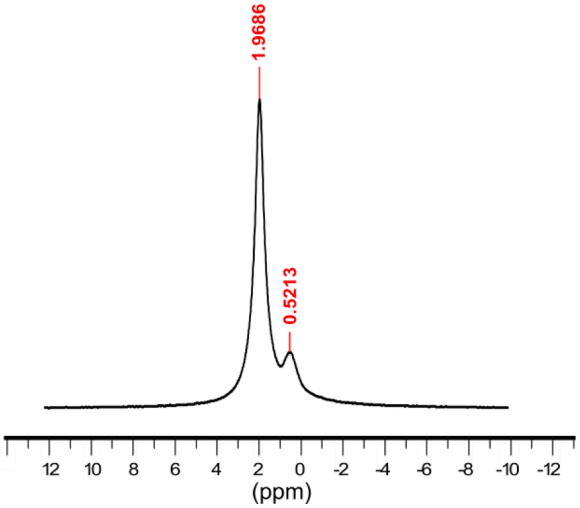

Fig. 3. ^{7}Li MAS NMR spectrum of the as synthesised L018STN showing the splitting of the main resonance.

shift is characteristic of diamagnetic materials [37]. In diamagnetic materials, a shift closer to 0 or towards negative values is indicative of a higher electron density at the lithium site, which results in an increased screening of the lithium nucleus. For example, the shift detected in lithium inserted anatase, Li_xTiO_2, has been associated with a closer proximity or a higher bonding of lithium to oxygen ions [38,39]. Thus, one can assign the two signals to lithium coordination by four (0.5213 ppm) and three (1.9686 ppm) oxygen atoms. This assignment falls in line with the NPD data where the position of Li is better defined at the square windows (Li1), but a bigger amount of Li is spread over Li2 sites.

The shift towards negative values indicate that lithium electron density is higher on the four coordinated site. Differences detected in NMR and ND intensity of two species suggest the partial onset of Li exchange between the sites during the NMR experiments.

To further rationalise the room temperature NMR and low temperature NPD data, ab initio MD calculations were performed. The structural relaxation of the above described 3 × 4 × 3 supercell show that with increasing Li content the Li atoms preferentially move towards the oxygen window. In fact, for the case of each A site being occupied by two Li atoms, all Li atoms are close to the oxygen window. This can be inferred from the two structures with increasing Li content depicted in Fig. S3A-D. Here, it is also interesting to note that the Ti/Nb-O framework is not significantly distorted under Li insertion and that Sr remains in the cavity center. Only at the highest Li content some Sr are slightly shifted away from the central position. To gain insight into the dynamics of Li, AIMD simulations were conducted for the two supercells with $Li_{0.17}Sr_{0.67}Ti_{0.5}Nb_{0.5}O_3$ and $Li_{0.5}Sr_{0.67}Ti_{0.5}Nb_{0.5}O_3$ stoichiometry. To determine the average Li distribution, the Li positions of the different Li atoms in the supercell were extracted throughout the AIMD simulation and then projected onto a single perovskite unit cell. Furthermore, the cubic symmetry of the perovskite was taken into account for all extracted Li sites. From the obtained distribution of Li in the perovskite unit cell a probability density could then be determined as shown in Fig. 4. From the isosurfaces it is also clear that most lithium is located in a position off-set from the O_4 window with the average distance to the O_4 window of the center of lithium probability decreasing with increasing Li content. Interestingly, the lithium density decreases within the center of the O_4 window.

Taking the three results together, at room temperature it is likely that lithium is largely located in a mobile disordered state within the *A*-site cavity with a higher probability of remaining on the 6c site with rapid hopping via the 8g site as a local energy minimum. This agrees with previous reports of lithium off-set from the O_4 window in defect LLTO and $Li_xLa_{1/3}NbO_3$ (LLNO) perovskites [40–45]. Further, for lithium intercalation into the Ruddlesen-Popper phase, $Y_2Ti_2O_5S_2$, the lithium was also found in the O_4 window position between *A*-site cavities within the perovskite layer [46]. While the center of the *A*-site cavity has been previously reported for these compounds as well [47–49], investigations on L018STN [22] have shown that the *A*-site center is not feasible due to underbonding of lithium.

3.2. Over-lithiation behaviour and lithium mobility

Morphology of pristine composite L018STN electrode used in this study was as depictured in SEM images (Fig.s S7C and S7D). To explore the reversibility of electrochemical cycling into the "over-lithiation" region of L018STN, galvanostatic cycling was performed down to 0.25 V. Due to side reactions of the ethylene carbonate which typically occur on lithiation between 0.7-0.8 V [50], some capacity was lost over the first 10 cycles. Similar reactions of ethylene carbonate forming an SEI have been observed with $Li_4Ti_5O_{12}$ [51]. The capacity stabilised at 62.9 ± 0.3 $mAhg^{-1}$ over the subsequent 60 cycles, corresponding to the reversible insertion of 0.42 Li^+ per FU (Fig. 5).

Considering the chemical formula of the compound, $Li_{0.18}Sr_{0.66}Ti_{0.5}Nb_{0.5}O_3$, there are 0.34 *A*-sites not occupied by Sr^{2+} of which 0.18 are occupied by Li^+, leaving 0.16 vacant *A*-site positions. If an additional 0.42 Li^+ per FU are reversibly inserted into the material, then at least 0.26 *A*-site cavities must contain two Li^+ ions. The ability to insert two lithium ions for each *A*-site has been demonstrated experimentally in L018STN, $Li_{0.5}La_{0.5}TiO_3$ and $Li_{0.35}La_{0.55}TiO_3$ [13,16,24] and simulations for $Li_{1.5}La_{1.5}WO_6$ show the possibility to electrochemically insert three or four Li^+ per *A*-site when lithiatied to 0.77 and 0.08 V, respectively [15]. If at most two lithium ions can occupy each *A*-site cavity, the maximum amount of lithium that can be inserted (x in $Li_{0.18+x}Sr_{0.66}Ti_{0.5}Nb_{0.5}O_3$) corresponds to 0.5 Li^+/FU with an expected capacity of 75.5 $mAhg^{-1}$. Thus, on lithiation to 0.25 V, 84% (~63 $mAhg^{-1}$) of the maximum capacity has been reversibly cycled.

Previously, when investigating the structural changes occurring on lithiation below 1 V using *operando* X-ray diffraction, two cubic perovskite phases, one more lithiated than the other, were observed [24]. The phase segregation was explained by assuming that upon insertion of more than one lithium per vacant site during lithiation, electrostatic repulsion between neighbouring Li^+ ions leads to an increase of the bulk resistance, creating a "reaction front" within individual particles. A similar phenomenon has been recently reported in $LiNi_{0.8}Mn_{0.1}Co_{0.1}O_2$, albeit at high states of delithiation [52]. The phase segregation in this previous work was ascribed to a decrease of lithium mobility in fatigued cells. ICI measurements were performed during galvanostatic cycling to explore the possibility of a loss of Li^+ mobility leading to the observed

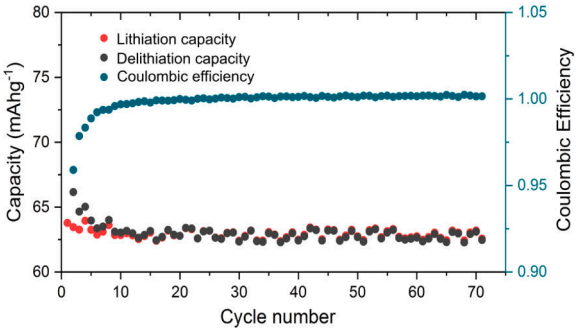

Fig. 5. Electrochemical characterization of L018STN illustrating the Coulombic efficiency and the capacity fading in a Li half-cell using 1 M $LiPF_6$ in 1:1 vol EC:DEC.

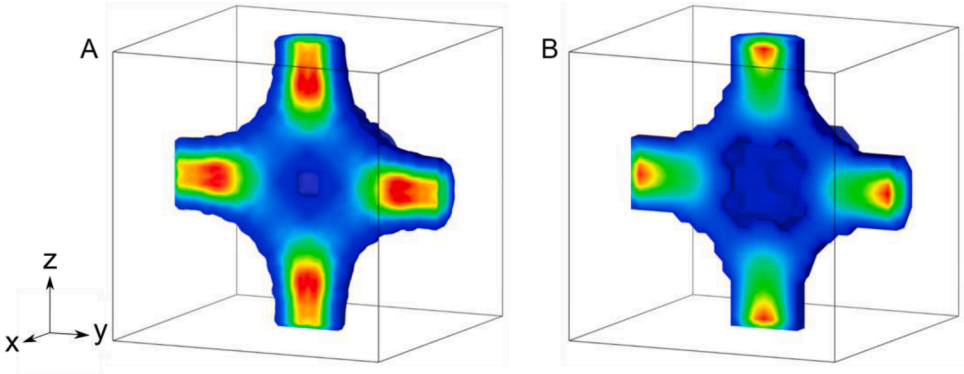

Fig. 4. Average Li distribution for A: $Li_{0.17}Sr_{0.67}Ti_{0.5}Nb_{0.5}O_3$ and B: $Li_{0.5}Sr_{0.67}Ti_{0.5}Nb_{0.5}O_3$ compounds obtained from AIMD simulations at 500 K. The isosurface plots have been cut at x=0.5 to reveal the cross-section of lithium density within the unit cell with red regions indicating high density and blue low density.

phase segregation.

The variation of internal resistance and lithium mobility with the potential is depicted in Fig. 6 as a function of inserted lithium content, x, in $Li_{0.18+x}Sr_{0.66}Ti_{0.5}Nb_{0.5}O_3$. Due to the irreversible capacity in the initial formation cycles, the first cycle voltage, resistance and lithium mobility has not been included in Fig. 6 but is provided in Fig. S5. The most notable change is that the lithium mobility decreases by half an order of magnitude during lithiation at ~0.25 Li^+/FU (average *A*-site occupancy of 1.26 Li), reaching a minimum at 0.34-0.36 Li^+/FU (average *A*-site occupancy of ~1.56 Li). This decrease in lithium mobility becomes less noticeable after extensive cycling and is not detected during the delithiation processes (*i.e.* Li^+ removal). On the contrary, the lithium mobility is an order of magnitude higher in the beginning of charging, which supports the hypothesis that resistance to diffusion increases during lithium insertion beyond 1 Li^+ per vacant site due to electrostatic repulsion [24]. Alleviation of this electrostatic repulsion during lithium removal would facilitate boosted lithium mobility at the beginning of the delithiation cycle. Indeed, in the previous study where this mechanism was proposed, the hysteresis was observed through a faster change of unit cell parameters during the subsequent delithiation for the same current density [24]. Interestingly, the lithium mobility is restored at ~0.4 Li^+/FU (average *A*-site occupancy of 1.71 Li) during lithiation. This may be due to a structural rearrangement of lithium and shift of diffusion mechanism from site percolation to bond percolation [53]. To explore this possibility and build an understanding of the changing local environment for Li, ^{7}Li NMR was employed. To support the interpretation of these data, changes to the oxidation state of titanium and niobium will first be examined since changes induced to the electronic structure during reduction can influence the ^{7}Li mobility as measured by NMR [7,8].

3.3. Oxidation state changes

Cyclic voltammetry measurements (Fig. 7A) performed on L018STN during the first five cycles show two highly reversible peaks at ~1.6 V and ~1.2 V. Previously, it has been measured in LLTO that Ti reduction can begin between 1.1-1.55 V, whereas for LLNO Nb reduction was observed to begin around 2 V [12,54–56]. Thus, one could expect that the higher potential peak would correspond to Nb reduction. However, the reduction potentials of Ti and Nb span a wide potential window and overlap to some degree. Further, LSTN which contains a random distribution of equal proportions of Ti and Nb over the *B*-site would lead to any Li inserted into the structure lying adjacent to either Ti or Nb with equal probability. Therefore, to confirm the reduction sequence in LSTN, oxidation states of Ti and Nb were directly measured using XPS on electrodes cycled to different potentials. Fitted XPS data presented in Fig. S6 show that both titanium and niobium are active at all potentials on lithiation and delithiation. Due to the SEI formation from decomposition of EC in the electrolyte, the Ti signal-to-noise ratio was reduced at potentials below 1 V during the lithiation processes.

To assess the proportion of active Ti and Nb, average oxidation states were estimated from the relative area of Nb^{5+}/Nb^{4+} and Ti^{4+}/Ti^{3+} signals. The absolute value of the difference between the average of the measured oxidation state and maximum possible oxidation state for each element was plotted (Fig. 7B) as a function of Li^+ content, x, as deduced from the total current passed during electrode preparations. Data correspond to electrodes lithiated to 1 V. Below 1 V, the reduction of the electrolyte consumes some of the charge passed, leading to an over estimation of lithium content in the first few cycles. If all current applied during lithiation contributed to redox reactions of the active material, the sum of oxidation state change for Ti and Nb must match the estimated Li^+ content. This is depicted by the dotted line passing through zero with a slope of 1, in Fig. 7B. For low Li^+ contents (delithiated state), the low intensity of Ti^{3+} and Nb^{4+} signals will increase the errors on estimating these values. As the Ti signal quality decreases during the lithiation processes, an additional source of error is produced. Considering these, total oxidation state change is within error being equal to the inserted lithium. Consequently, as the sum lies above the

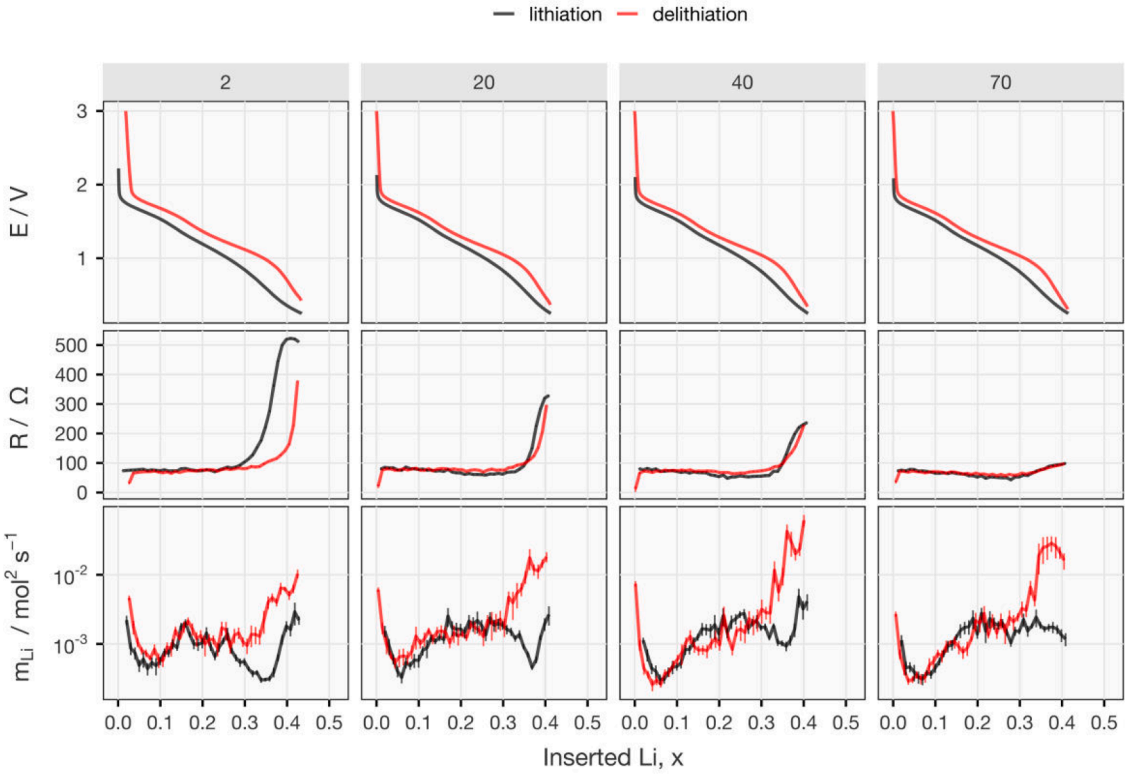

Fig. 6. The potential (E), internal resistance (R), and lithium mobility (m_{Li}) plotted against inserted Li^+ content (x) for the cycles 2, 20, 40 and 70 (indicated on top of the Fig. with numerals) measured during the galvanostatic cycling of L018STN in a half cell against Li metal using 1 M $LiPF_6$ in 1:1 vol EC:DEC.

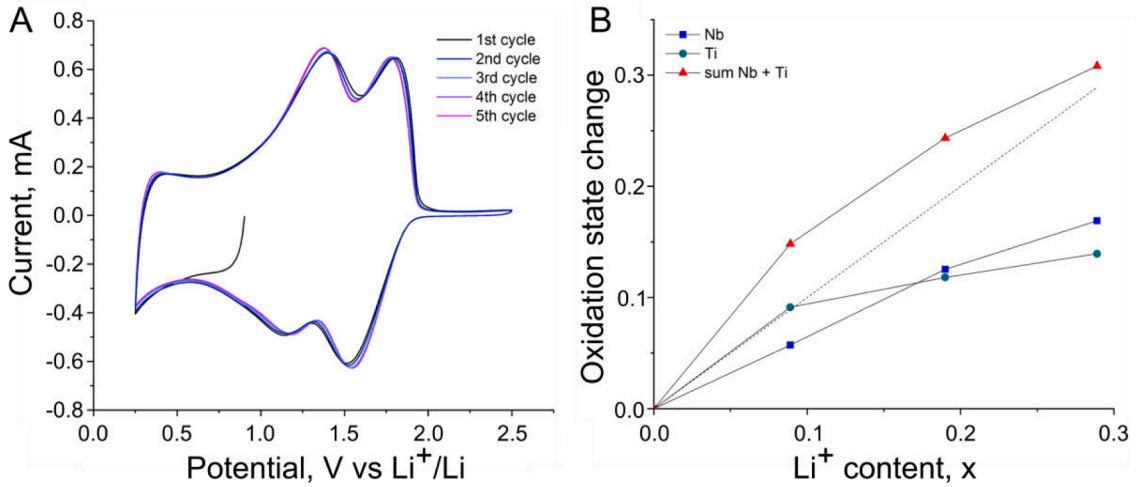

Fig. 7. A: Cyclic voltammograms of L018STN electrode at a scan rate of 0.5 mV s^{-1} between 0.25 and 2.5 V (vs. Li^+/Li) for the first five cycles. **B:** Change in oxidation state for Nb and Ti (and their sum) relative to the 5+ and 4+ states respectively plotted against the lithium content x in $Li_{0.18+x}Sr_{0.66}Ti_{0.5}Nb_{0.5}O_3$. The dotted line corresponds to the limit where the total oxidation state change equals the measured lithium content change.

dotted line, side reactions or non-faradaic processes do not significantly contribute to the observed capacity. Further, Nb and Ti signals change at approximately the same rate during lithium insertion, contrary to initial predictions. The difference between the CV and XPS results can also be influenced by the CV being measured on the material during operation in a battery whereas the XPS measured *ex situ* on samples that have structurally relaxed.

3.4. Lithium environment following over-lithiation

The Li bands in the ^7Li NMR spectra of the electrochemically lithiated samples are split into two resonances, one of which is more negatively shifted with respect to the as prepared samples (Fig. 8A). The insertion of Li^+ is accompanied by the formation of more Ti^{3+} and Nb^{4+} and thus unpaired electron spin density is transferred from Ti^{3+}/Nb^{4+} via oxygen to the Li^+ nuclei resulting in a right shift of the ^7Li NMR peaks [37,57]. As shown in the previous section titanium and niobium are electrochemically active in L018STN at all potentials. As more lithium is inserted into L018STN, a larger proportion of cations are reduced creating a more negative shift of peaks corresponding to the lithium environments. However, the extent of the shift becomes less pronounced for lower potentials. At 1.630 V two resonances at 2.3(2) and -7.14(1) ppm are resolved. Based on the electrochemical tests performed, this potential corresponds to ~0.07 Li^+/FU inserted which is below one lithium per available *A*-site. The two peaks observed in the spectra reveal shifts that are larger than those typically observed for diamagnetic samples (+/- 5 ppm [37]). The presence of two peaks reveals two different Li environments caused by different Ti^{4+}/Ti^{3+} or Nb^{5+}/Nb^{4+} neighbour arrangements. As the lithium insertion follows a solid solution type reaction mechanism it can be assumed that these two sites co-exist in one phase.

It is surprising that the insertion of additional lithium does not cause any additional changes below 1.434-1.382 V, especially considering the increased presence of d^1 cations. Specifically, an additional resonance corresponding to lithium ions in proximity of paramagnetic cations was expected. There are three possibilities that can be considered based on other defect perovskites. In lithium inserted $La_{0.59}Li_{0.24}TiO_3$, the observed signal intensity decreased sharply [57]. In this case, new and strong coupling would lead to ^7Li nuclei to become unobservable. Alternatively, if the reduced cations are too far away from the inserted or original lithium ions the influence of the paramagnetic cations would be reduced. It has been shown for $Li_{0.066}La_{0.64}TiO_3$ that the titanium atoms gain electrons independent of the lithium position and the same could

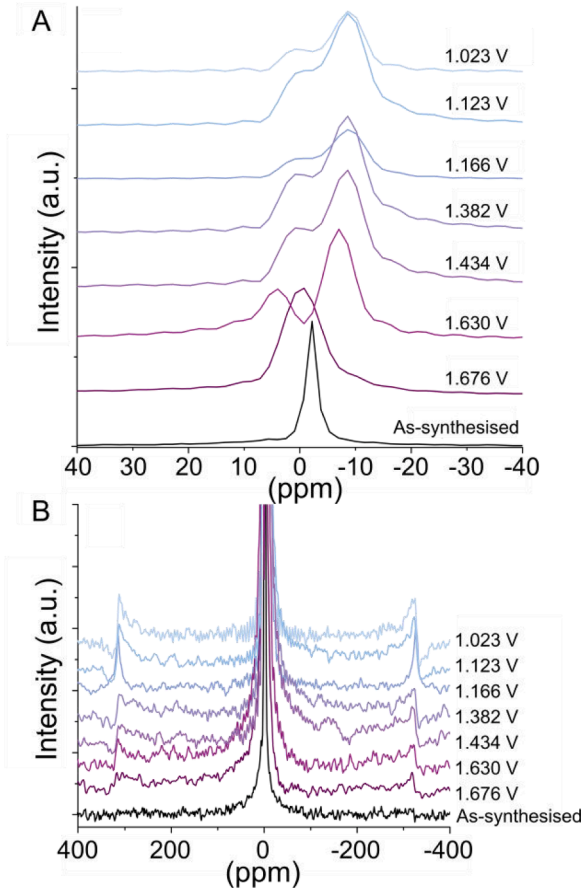

Fig. 8. A: Central transition from the ^7Li MAS NMR spectra of several $Li_{0.18+x}Sr_{0.66}Ti_{0.5}Nb_{0.5}O_3$ compounds lithiated to different potentials. The lower potential samples contain a higher amount of Li^+/FU **B:** View of the sideband region for the same samples. The side bands were detected at ±321 ppm.

happen here given the low Li^+ content inserted above 1 V [58]. A third possible explanation for the similar chemical shifts would be that the lithium mobility in the bulk material is high enough to decrease or average out paramagnetic interactions.

An additional spectral feature that changes with Li^+ insertion is the

linewidth of components. In the analyzed samples, linewidth increases at high voltage (low Li^+ content) but does not change significantly when lithiated to lower voltages (higher Li^+ content). As a narrower peak corresponds to increased lithium mobility, the reduction in lithium mobility occurs almost near the beginning of lithium insertion and then does not change down to ~1 V [20]. This reduction in lithium mobility also affects spinning side bands at ±321 ppm which increase in intensity (Fig. 8B). These side bands provide information on distortions in lithium coordination [37]. Their intensity decreases when the symmetry of the lithium environment or lithium mobility increases leading to decreased quadrupolar anisotropies [19]. As L018STN exhibits broader peaks and more intense spinning side bands, it suggests that the lithium ions become less mobile [20,57,59]. This observation agrees with the results in Fig. 6 which show a drop in Li^+ mobility at the beginning of lithiation that does not significantly vary to 1 V.

Interestingly, most ^{7}Li MAS NMR studies of defect perovskites have not obtained results similar to those described here, specifically, the observation of a single central resonance formed by two components corresponding to lithium ions with different mobilities. Previously, it has been concluded that the resonances arise from lithium in two different *A*-site layers, for example of the LLTO and LLNO series [18,20,40,41,43,54,58,60,61] . However, for L018STN with a random distribution of *A*-site vacancies, there is no difference in contiguous *A*-site layers. Thus, one would expect a result similar to the cubic $Li_{0.5}La_{0.5}TiO_3$ perovskite which only exhibits a single resonance, corresponding to a single lithium environment [5,6]. Similarly, quenched $Li_{0.18}La_{0.61}TiO_3$ with a rhombohedral unit cell also displays a single ^{7}Li NMR resonance [10]. The only study which shows several Li resonances was for $Li_{0.12}La_{0.21}NbO_3$ heated to 480 and then 800 K. In this case, it was concluded that one lithium environment was highly symmetric while the other two were more distorted [7].

4. Discussion

The results from this study combined with previous X-ray and neutron diffraction studies of chemically and electrochemically prepared LSTN, allow for a description of the lithium insertion and diffusion mechanism. In the as-synthesised material there are two distinct lithium sites with a high degree of mobility between them at room temperature. These are the 8g site (coordinated by 3 oxygens from Ti/NbO_6 octahedra) and the 6f site (off-set from O_4 window). Thus, it is proposed that lithium rapidly moves from 8g-6f-8g within the *A*-site cavity and more slowly from 6f to 6f sites between *A*-site cavities via the O_4 window, which acts as a bottleneck (Fig. 1B). This diffusion pathway agrees with previous bond valence sum calculations and the DFT results presented here and can be described by site percolation. A similar model has been used to describe other lithium conducting perovskites with lithium located within the *A*-site cavity [17].

The lithium arrangement in L018STN is altered as soon as additional lithium is inserted into the structure with a higher population found on the 6f site offset from the O_4 window. The rearrangement coincides with a drop of local lithium mobility, as qualitatively determined via ^{7}Li NMR and quantitatively measured using the ICI technique. The mobility remains stable until an average occupancy of 1.26 Li^+/*A*-site where it drops significantly. Previous X-ray diffraction results of electrochemically prepared samples revealed that 0.52 out of 0.59 lithium ions per formula unit are found offset from the O_4 window [24]. Thus, as the lithium insertion process continues, gradual rearrangement occurs to maximize the distance between mobile lithium ions and minimize electrostatic repulsion. This process reaches a natural limit at higher lithium concentrations where further reorganization to minimize electrostatic repulsion is no longer possible and lithium mobility subsequently drops. However, previous neutron diffraction results from chemically prepared samples revealed that 0.25(2) out of 0.40 Li^+/FU, are positioned in the centers of the O_4 windows between *A*-sites (3c site: 0.5 0.5 0) [22] . Thus, with sufficient local electrostatic repulsion combined with elongation of the Ti/Nb-O bonds and expansion of the O_4 window during reduction, lithium is forced into the window site modifying the diffusion mechanism from site percolation to bond percolation (Fig. 1B). Lithium diffusion via bond percolation is the explanation for why defect perovskites such as rhombohedral and orthorhombic $Li_{0.5}La_{0.5}TiO_3$ exhibit higher Li^+ ion diffusion than is predicted by the site percolation model [18,60]. Further, as 0.18 Li^+/FU are never extracted from the compound it is predicted that over time these lithium ions become pinned in the O_4 window, maintaining some degree of bond percolation at the end of the charging process. The change in diffusion mechanism can explain the increase in lithium mobility measured by ICI once the lithium content exceeds ~1.56 Li^+/*A*-site and that after 70 cycles a loss of mobility during lithiation is no longer observed.

Finally, alleviation of the Li-Li repulsion at the beginning of charging is proposed to be responsible for the sharp increase of lithium mobility as measured using ICI. The sharp loss of Li^+ mobility during lithiation and gain during delithiation is likely the reason behind the kinetically driven phase separation, which exhibited similar hysteresis between lithiation and delithiation [24].

5. Conclusions

The changing environment for lithium ions in defect perovskite $Li_{0.18}Sr_{0.66}Ti_{0.5}Nb_{0.5}O_3$ (L018STN) has been determined as a function of lithium content and for the first time correlated to the evolving resistance and lithium mobility. The lithium was found randomly distributed over the 8g site (off-set from Ti/NbO_6 octahedral face) and the 6f site (off-set from O_4 window) in the as-synthesised compound. During lithiation, electrostatic repulsion from the additional lithium forces more of the lithium onto the 6f site which coincides with a drop of lithium mobility. This drop of mobility reaches a critical point beyond an average *A*-site lithium occupancy of 1.25 reaching a minimum at 1.56 Li^+/*A*-site. Intriguingly, the lithium mobility is also restored during over-lithiation to 1.71 Li^+/*A*-site and the loss of mobility is reduced on every subsequent cycle. It is suggested that further lithium reorganisation occurs with pinning in the O_4 window (0.5 0.5 0) site. The shift of Li^+ position alleviates local electrostatic repulsion effects and modifies the diffusion behaviour from site percolation to bond percolation. These results reveal a constantly changing lithium position and diffusion behaviour in the short and long term with respect to electrochemical cycling with a general trend towards increased lithium mobility. Therefore, the design of defect perovskites with lithium already in the *A*-site window appears to be a feasible strategy to immediately access higher mobility and cycling stability in high-capacity defect perovskite electrodes. Beyond this practical observation, the results provide insight into the driving forces behind non-equilibrium transformations occurring within electrode materials during repeated lithium insertion and removal.

CRediT authorship contribution statement

William R. Brant: Writing – original draft, Conceptualization, Methodology, Writing – review & editing. **Tatiana Koriukina:** Investigation, Formal analysis, Writing – review & editing. **Yu-Chuan Chien:** Investigation, Formal analysis. **Holger Euchner:** Investigation, Formal analysis. **Jesus Sanz:** Investigation, Formal analysis. **Alois Kuhn:** Investigation, Formal analysis. **Ralf Heinzmann:** . **Sylvio Indris:** Investigation, Formal analysis. **Siegbert Schmid:** Resources, Supervision, Writing – review & editing.

Declaration of Competing Interest

The authors declare that they have no known competing financial interests or personal relationships that could have appeared to influence the work reported in this paper.

The authors declare the following financial interests/personal relationships which may be considered as potential competing interests:.

Data availability

Data will be made available on request.

Acknowledgments

W.R.B., T.K. and Y-C. C. are grateful to the strategic research area StandUp for Energy for financial support. A.K. and J.S. thank the Agencia Estatal de Investigación (AEI) / Fondo Europeo de Desarrollo Regional (FEDER/UE) for funding the project PID2019-106662RB-C41,2. A part of this work was carried out on the ECHIDNA neutron diffraction instrument at the OPAL reactor, Australian Nuclear Science and Technology Organisation and the authors would like to acknowledge the technical support provided by instrument staff. The authors would like to thank AINSE Ltd for providing financial assistance through the postgraduate award and research fellowship schemes. The authors would also like to acknowledge the technical support from the School of Chemistry at the University of Sydney. The authors also acknowledge Myfab Uppsala for providing facilities and experimental support. Myfab is funded by the Swedish Research Council as a national research infrastructure.

Supplementary materials

Supplementary material associated with this article can be found, in the online version, at doi:10.1016/j.electacta.2022.141759.

References

[1] Y. Inaguma, L. Chen, M. Itoh, T. Nakamura, High lithium ion conductivity in the perovskite-type compounds, Solid State Commun. 86 (10) (1993) 689–693 [Online]. Available, http://linkinghub.elsevier.com/retrieve/pii/0167273894903107.

[2] A. G. Belous, G. N. Novitskaya, S. v. Polyanetskaya, and Yu. I. Gornikov, "Investigation into complex oxides of La2/3-xLi3xTiO3 composition," *Izvestiia Akademii nauk SSSR. Neorganicheskie materialy.*, vol. 23, pp. 470–472, 1987, Accessed: Nov. 18, 2021. [Online]. Available: https://inis.iaea.org/search/search.aspx?orig_q=RN:18094031.

[3] D. Stauffer, A. Aharony, Introduction To Percolation Theory, 2nd Editio, Taylor & Francis, London, 2017, https://doi.org/10.1201/9781315274386.

[4] M. Morcrette, et al., In situ X-ray diffraction techniques as a powerful tool to study battery electrode materials, Electrochim. Acta 47 (19) (2002) 3137–3149, https://doi.org/10.1016/S0013-4686(02)00233-5.

[5] Y. Inaguma, Y. Matsui, J. Yu, Y.J. Shan, T. Nakamura, M. Itoh, Effect of substitution and pressure on lithium ion conductivity in perovskites Ln1/2Li1/2TiO3 (Ln = La, Pr, Nd and Sm), J. Phys. Chem. Solids 58 (6) (1997) 843–852, https://doi.org/10.1016/S0022-3697(96)00226-0.

[6] L. Latie, G. Villeneuve, D. Conte, G. le Flem, Ionic conductivity of oxides with general formula LixLn1/3Nb1-xTixO3 (Ln = La, Nd), J. Solid State Chem. 51 (3) (1984) 293–299, https://doi.org/10.1016/0022-4596(84)90345-1.

[7] H.T. Chung, J.G. Kim, H.G. Kim, Dependence of the lithium ionic conductivity on the B-site ion substitution in (Li0.5La0.5)Ti1 - XMxO3 (M = Sn, Zr, Mn, Ge), Solid State Ionics 107 (1–2) (1998) 153–160, https://doi.org/10.1016/s0167-2738(97)00525-0.

[8] S. Stramare, V. Thangadurai, W. Weppner, Lithium lanthanum titanates: a review, ChemInform 34 (52) (2003), https://doi.org/10.1002/chin.200352244.

[9] P. Birke, S. Scharner, R.A. Huggins, W. Weppner, Electrolytic stability limit and rapid lithium insertion in the fast-ion-conducting Li0.29La0.57TiO3 perovskite-type compound, J. Electrochem. Soc. 144 (6) (1997) L167–L169, https://doi.org/10.1149/1.1837713.

[10] Y. Inaguma, L. Chen, M. Itoh, T. Nakamura, Candidate compounds with perovskite structure for high lithium ionic conductivity, Solid State Ionics 70–71 (1994) 196–202, https://doi.org/10.1016/0167-2738(94)90309-3.

[11] C. Bohnke, O Bohnke, J.L. Fourquet, Mechanism of ionic conduction and electrochemical intercalation of lithium into the perovskite lanthanum lithium titanate, Solid State Ionics 91 (1996) 21–31.

[12] F. García-Alvarado, A. Várez, E. Morán, M.A. Alario-Franco, Structural details and lithium intercalation in the perovskite La0.5Li0.5TiO3, Phase Transitions 58 (1–3992) (1996) 111–120, https://doi.org/10.1080/01411599608242397.

[13] C.H. Chen, K. Amine, Ionic conductivity, lithium insertion and extraction of lanthanum lithium titanate, Solid State Ionics 144 (1–2) (2001) 51–57, https://doi.org/10.1016/S0167-2738(01)00884-0.

[14] Y. Inaguma, M. Itoh, Influences of carrier concentration and site percolation on lithium ion conductivity in perovskite-type oxides, Solid State Ionics 86–88 (PART 1) (1996) 257–260, https://doi.org/10.1016/0167-2738(96)00100-2.

[15] M. Amores, et al., Li1.5La1.5 MO6 (M = W6+, Te6+) as a new series of lithium-rich double perovskites for all-solid-state lithium-ion batteries, Nat. Commun. 11 (1) (2020) 1–12, https://doi.org/10.1038/s41467-020-19815-5.

[16] L. Zhang, et al., Lithium lanthanum titanate perovskite as an anode for lithium ion batteries, Nat. Commun. 11 (1) (2020) 1–8, https://doi.org/10.1038/s41467-020-17233-1.

[17] Y. Inaguma, Fast Percolative Diffusion in Lithium Ion-conducting Perovskite-type Oxides, J. Ceram. Soc. Jpn. 114 (12) (2006) 1103–1110. *114*.

[18] M. Yashima, M. Itoh, Y. Inaguma, Y. Morii, Crystal structure and diffusion path in the fast lithium-ion conductor La0.62Li0.16TiO3, J. Am. Chem. Soc. 127 (10) (2005) 3491–3495, https://doi.org/10.1021/ja0449224.

[19] A. Rivera, et al., Percolation-limited ionic diffusion in Li0.5-xNaxLa0.5TiO3 Perovskites (0 ≤ x ≤ 0.5), Chem. Mater 14 (2002) 5148–5152, https://doi.org/10.1021/cm0204627.

[20] J. Ibarra, A. Várez, C. León, J. Santamaría, L.M. Torres-Martínez, J. Sanz, Influence of composition on the structure and conductivity of the fast ionic conductors La2/3-xLi3xTiO3 (0.03≤x≤0.167, Solid State Ionics 134 (3–4) (2000) 219–228, https://doi.org/10.1016/S0167-2738(00)00761-X.

[21] W. Bucheli, et al., Near constant loss regime in fast ionic conductors analyzed by impedance and NMR spectroscopies, Phys. Chem. Chem. Phys. 16 (29) (2014) 15346–15354, https://doi.org/10.1039/c4cp01773k.

[22] W.R. Brant, et al., Rapid lithium insertion and location of mobile lithium in the defect perovskite Li0.18Sr0.66Ti0.5Nb 0.5O3, ChemPhysChem 13 (9) (2012) 2293–2296, https://doi.org/10.1002/cphc.201200017.

[23] W.R. Brant, S. Schmid, Q. Gu, R.L. Withers, J. Hester, M. Avdeev, Temperature and composition dependent structural investigation of the defect perovskite series Sr1-xTi1-2xNb2xO 3, 0≤x≤0.2, J. Solid State Chem. 183 (9) (2010) 1998–2003, https://doi.org/10.1016/j.jssc.2010.06.002.

[24] W.R. Brant, D. Li, Q. Gu, S. Schmid, Comparative analysis of ex-situ and operando X-ray diffraction experiments for lithium insertion materials, J. Power Sources 302 (2016) 126–134, https://doi.org/10.1016/j.jpowsour.2015.10.015.

[25] W.R. Brant, et al., A large format in operando wound cell for analysing the structural dynamics of lithium insertion materials, J. Power Sources 336 (2016) 279–285, https://doi.org/10.1016/j.jpowsour.2016.10.071.

[26] M.J. Lacey, Influence of the electrolyte on the internal resistance of lithium−sulfur batteries studied with an intermittent current interruption method, ChemElectroChem 4 (8) (2017) 1997–2004, https://doi.org/10.1002/celc.201700129.

[27] Y.C. Chien, A.S. Menon, W.R. Brant, D. Brandell, M.J. Lacey, Simultaneous monitoring of crystalline active materials and resistance evolution in lithium-sulfur batteries, J. Am. Chem. Soc. 142 (3) (2020) 1449–1456, https://doi.org/10.1021/jacs.9b11500.

[28] Y.-C. Chien, H. Liu, A. S. Menon, W. R. Brant, D. Brandell, and M. J. Lacey, "A Fast Alternative To The Galvanostatic Intermittent Titration Technique," ChemRxiv, 2021. This content is a preprint and has not been peer-reviewed. doi: 10.33774/chemrxiv-2021-09srz.

[29] K.D. Liss, B. Hunter, M. Hagen, T. Noakes, S. Kennedy, Echidna-the new high-resolution powder diffractometer being built at OPAL, Physica B 385–386 (2006) 1010–1012, https://doi.org/10.1016/j.physb.2006.05.322.

[30] N. Fairely, "CasaXPS Manual 2.3. 15 Getting started with CasaXPS," Casa Software Ltd, pp. 1–177, 2009, [Online]. Available: http://scholar.google.com/scholar?hl=en&btnG=Search&q=intitle:CasaXPS+Manual+2.3.15#2.

[31] J. Kresse, G. Furthmüller, Efficient iterative schemes for ab initio total-energy calculations using a plane-wave basis set, Phys. Rev. B 54 (1996) 11169, https://doi.org/10.1103/PhysRevB.54.11169.

[32] D. Kresse, G. Joubert, From ultrasoft pseudopotentials to the projector augmented-wave method, Phys. Rev. B - Condensed Matter Materials Physics 59 (3) (1999) 1758–1775, https://doi.org/10.1103/PhysRevB.59.1758.

[33] J.P. Perdew, K. Burke, M. Ernzerhof, Generalized gradient approximation made simple, Phys. Rev. Lett. 77 (18) (1996) 3865–3868, https://doi.org/10.1103/PhysRevLett.77.3865.

[34] J. E, Alex Zunger, S.-H. Wei, L.G. Ferreira, Bernard, Special quasirandom structures, Phys. Rev. Lett. 65 (1990) 353, https://doi.org/10.1103/PhysRevLett.65.353.

[35] A. van de Walle, et al., Efficient stochastic generation of special quasirandom structures, CALPHAD: Comput. Coupling Phase Diagrams Thermochem. 42 (2013) 13–18, https://doi.org/10.1016/j.calphad.2013.06.006.

[36] A.B. Santibáñez-Mendieta, et al., La3Li3W2O12: ionic diffusion in a perovskite with lithium on both A- and B-sites, Chem. Mater. 28 (21) (2016) 7833–7851, https://doi.org/10.1021/acs.chemmater.6b03220.

[37] C.P. Grey, N. Dupré, NMR studies of cathode materials for lithium-ion rechargeable batteries, Chem. Rev. 104 (10) (2004) 4493–4512, https://doi.org/10.1021/cr020734p.

[38] M. Wagemaker, R. van de Krol, A.P.M. Kentgens, A.A. van Well, F.M. Mulder, Two phase morphology limits lithium diffusion in TiO2 (anatase): a 7Li MAS NMR study, J. Am. Chem. Soc. 123 (46) (2001) 11454–11461, https://doi.org/10.1021/ja0161148.

[39] V. Luca, T.L. Hanley, N.K. Roberts, R.F. Howe, NMR and X-ray absorption study of lithium intercalation in micro- and nanocrystalline anatase, Chem. Mater. 11 (8) (1999) 2089–2102, https://doi.org/10.1021/cm990007j.

[40] M. Catti, First-principles modeling of lithium ordering in the LLTO (Li xla2/3-x/3TiO3) superionic conductor, Chem. Mater. 19 (16) (2007) 3963–3972, https://doi.org/10.1021/cm0709469.

[41] M. Sommariva, M. Catti, Neutron diffraction study of quenched Li0.3la 0.567TiO3 lithium ion conducting perovskite, Chem. Mater. 18 (9) (2006) 2411–2417, https://doi.org/10.1021/cm060120r.
[42] M. Nakayama, J. Shirakawa, M. Wakihara, Ab initio density functional study on changes in local structure in perovskite compound, LixLa1/3NbO3, Solid State Ionics 177 (15–16) (2006) 1259–1266, https://doi.org/10.1016/j.ssi.2006.06.028.
[43] J. Sanz, J.A. Alonso, A. Varez, M.T. Fernández-Díaz, Octahedral tilting and ordering of vacancies in the fast ion conductor Li0.12La0.63TiO3 perovskite: a neutron diffraction study, J. Chem. Soc. Dalton Trans. 7 (2002) 1406–1408, https://doi.org/10.1039/b109926b.
[44] T. Katsumata, Y. Inaguma, M. Itoh, K. Kawamura, Influence of covalent character on high Li ion conductivity in a perovskite-type Li ion conductor: prediction from a molecular dynamics simulation of La0.6Li0.2TiO3, Chem. Mater. 14 (9) (2002) 3930–3936, https://doi.org/10.1021/cm0203969.
[45] Y. Inaguma, T. Katsumata, M. Itoh, Y. Morii, Crystal structure of a lithium ion-conducting perovskite La2/3-xLi3xTiO3 (x = 0.05, J. Solid State Chem. 166 (1) (2002) 67–72, https://doi.org/10.1006/jssc.2002.9560.
[46] G. Hyett, O.J. Rutt, Z.A. Gál, S.G. Denis, M.A. Hayward, S.J. Clarke, Electronically driven structural distortions in lithium intercalates of the n = 2 ruddlesden-popper-type host Y2Ti2O 5S2: synthesis, structure, and properties of Li xY2Ti2O5S2 (0 < x < 2), J Am Chem Soc 126 (7) (2004) 1980–1991, https://doi.org/10.1021/ja037763h.
[47] R.A. Dilanian, A. Yamamoto, F. Izumi, T. Kamiyama, Crystal structures and resistivities of La1/3LixNbO3, Molecular Crystals and Liquid Crystals Science and Technology Section A: Molecular Crystals and Liquid Crystals 341 (2000) 225–230, https://doi.org/10.1080/10587250008026144.
[48] A.I. Ruiz, M.L. López, M.L. Veiga, C. Pico, Structural refinement by neutron diffraction of La1.12Li0.62Ti2O6, J. Solid State Chem. 148 (2) (1999) 329–332, https://doi.org/10.1006/jssc.1999.8456.
[49] J.L. Fourquet, H. Duroy, M.P. Crosnier-Lopez, Structural and Microstructural Studies of the Series $La_{2/3-x}$ $Li_{3x\square 1/3-2x}$ TiO_3, J. Solid State Chem. 127 (1996) (1996) 283–294.
[50] C. Shen, S. Wang, Y. Jin, W.Q. Han, In Situ AFM imaging of solid electrolyte interfaces on HOPG with ethylene carbonate and fluoroethylene carbonate-based electrolytes, ACS Appl. Mater. Interfaces 7 (45) (2015) 25441–25447, https://doi.org/10.1021/acsami.5b08238.
[51] S. Wang, K. Yang, F. Gao, D. Wang, C. Shen, Direct visualization of solid electrolyte interphase on Li4Ti5O12 by: In situ AFM, RSC Adv. 6 (81) (2016) 77105–77110, https://doi.org/10.1039/c6ra16208h.
[52] C. Xu, et al., Bulk fatigue induced by surface reconstruction in layered Ni-rich cathodes for Li-ion batteries, Nat. Mater. 20 (1) (2021) 84–92, https://doi.org/10.1038/s41563-020-0767-8.
[53] J. Wu, et al., A review on structural characteristics, lithium ion diffusion behavior and temperature dependence of conductivity in perovskite-type solid electrolyte Li3xLa2/3-x TiO3, Functional Mater. Lett. 10 (3) (2017), https://doi.org/10.1142/S179360471730002X.
[54] A. Kuhn, F. García-Alvarado, A. Varez, J. Sanz, Influence of Percolation Effects on Lithium Intercalation into Li[sub 0.5−x]Na[sub x]La[sub 0.5]TiO[sub 3] (0≤x≤0.5) Perovskites, J. Electrochem. Soc. 152 (12) (2005) A2285, https://doi.org/10.1149/1.2073107.
[55] Y.J. Shan, L. Chen, Y. Inaguma, M. Itoh, T. Nakamura, Oxide cathode with perovskite structure for rechargeable lithium batteries, J. Power Sources 54 (2) (1995) 397–402, https://doi.org/10.1016/0378-7753(94)02110-O.
[56] A. Nadiri, G. le Flem, C. Delmas, Lithium intercalation in Ln1/3NbO3 perovskite-type phases (Ln = La, Nd), J. Solid State Chem. 73 (2) (1988) 338–347, https://doi.org/10.1016/0022-4596(88)90118-1.
[57] J. Emery, O. Bohnke, J.L. Fourquet, J.Y. Buzaré, P. Florian, D. Massiot, Polaronic effects on lithium motion in intercalated perovskite lithium lanthanum titanate observed by 7Li NMR and impedance spectroscopy, J. Phy. Condensed Matter 11 (50) (1999) 10401–10417, https://doi.org/10.1088/0953-8984/11/50/330.
[58] M. Nakayama, T. Usui, Y. Uchimoto, M. Wakihara, M. Yamamoto, Changes in electronic structure upon lithium insertion into the a-site deficient perovskite type oxides (Li,La)TiO3, J. Phys. Chem. B 109 (9) (2005) 4135–4143, https://doi.org/10.1021/jp046062j.
[59] J. Emery, J.Y. Buzare, O. Bohnke, J.L. Fourquet, Lithium-7 NMR and ionic conductivity studies of lanthanum lithium titanate electrolytes, Solid State Ionics 99 (1–2) (1997) 41–51, https://doi.org/10.1016/s0167-2738(97)00202-6.
[60] J.A. Alonso, J. Sanz, J. Santamaría, C. León, A. Várez, M.T. Fernández-Díaz, On the location of Li+ cations in the fast Li-cation conductor La0.5Li0.5TiO3 perovskite, Angewandte Chemie - International Edition 39 (3) (2000) 619–621, https://doi.org/10.1002/(SICI)1521-3773(20000204)39:3<619::AID-ANIE619>3.0.CO;2-O.
[61] M. Catti, Ion mobility pathways of the Li+ conductor Li 0.125la0.625TiO3 by ab initio simulations, J. Phys. Chem. C 112 (29) (2008) 11068–11074, https://doi.org/10.1021/jp803345y.